Dynamic Similarity and Scale Effects in Turbulent Free-Surface Flows above Triangular Cavities

H. Chanson[1] and S. Felder[1]
[1]Division of Civil Engineering, The University of Queensland,
Brisbane QLD 4072, AUSTRALIA

Abstract

In high-velocity free-surface flows, air is continuously trapped and released through the interface, and the resulting air-water mixture are subjected to intense interactions between entrained air and turbulence. Two-phase flow properties were measured herein in high-velocity open channel flows above triangular cavities. Detailed turbulence measurements were conducted in a large-size facility to test the validity of the Froude and Reynolds similarities. The results showed consistently that the Froude similitude was not satisfied using a 2:1 geometric scaling ratio. Lesser number of entrained bubbles and comparatively greater bubble sizes were observed at the smaller Reynolds numbers, as well as lower turbulence levels and larger turbulent length and time scales. In practical terms, small-size models did underestimate the rate of energy dissipation and the aeration efficiency of prototype stepped spillways for similar flow conditions. Similarly a Reynolds similitude was tested. The results showed also some significant scale effects. However a number of self-similar relationships remained invariant under changes of scale and confirmed the analysis of Chanson and Carosi (2007). The finding is significant and suggests that self-similarity may provide a picture general enough to be used to characterise the air-water flow field in large prototype channels.

Introduction

In high-velocity free-surface flows, the strong interactions between the turbulent waters and the atmosphere lead to a strong air-water mixing at the interface. Through the free-surface, air is continuously trapped and released, and the resulting air-water mixture gives a whitish appearance to the entire flow (Fig. 1). The air-water flow motion is complicated (Rao and Kobus 1971, Kobus 1984, Wood 1991, Chanson 1997). The void fraction ranges from some small, often non-zero values close to the invert to 100% above the "free-surface" (e.g. Cain and Wood 1981). A key feature is the intense interactions between entrained air and turbulence (Brocchini and Peregrine 2002, Chanson and Toombes 2002). Presently, limited information is available on the two-phase flow properties of high-velocity free-surface flows, despite some milestone contributions (Straub and Anderson 1958, Cain and Wood 1981), in particular in terms of the turbulent properties. Recently Chanson and Carosi (2007) measured the turbulent length scales of large vortical structures advecting air bubbles in some skimming flows above a stepped spillway model. The size of these large eddies were closely related to the characteristic air–water depth Y_{90}. In the spray region, these results highlighted the existence of an upper spray region (C > 0.95–0.97) in which the distributions of droplet chord sizes and integral advection scales presented some marked differences with the rest of the flow.

In the present study, the two-phase flow properties of high-velocity open channel flows were studied experimentally. Detailed turbulence data were collected in a large-size channel with triangular cavities. The measurements were conducted with two cavity sizes and several discharges, and the data included turbulence levels and turbulent time and length scales. The

results were used to test the validity of the Froude and Reynolds similarities, and possible scale effects.

Fig. 1. Free-surface aeration in open channel flow down a staircase channel. Opuha dam spillway in operation (Courtesy of John Grimston and Tonkin and Taylor NZ).
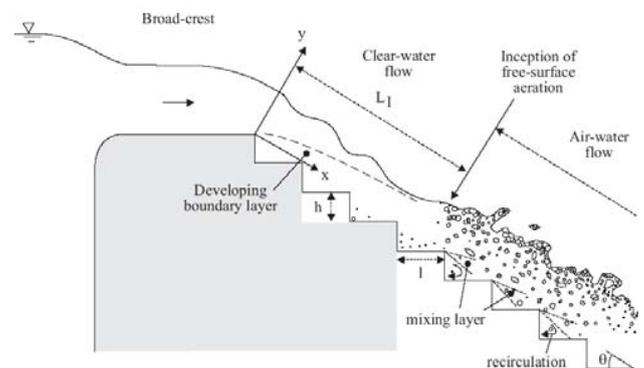

Fig. 2. Definition sketch of a skimming flow on a stepped channel.

Dimensional Analysis and Similitude

Considering a skimming flow in a rectangular channel equipped with triangular cavities (Fig. 2), a simple dimensional analysis gives a dimensionless relationship between the two-phase flow properties at a dimensionless location (x/d_c, y/d_c, z/d_c) and channel characteristics, inflow properties and fluid properties. It yields:

$$C, \frac{V}{\sqrt{g \times d_c}}, \frac{u'}{V}, T_{int} \times \sqrt{\frac{g}{d_c}}, \frac{L_{xz}}{d_c} = F\left(\frac{x}{d_c}, \frac{y}{d_c}, \frac{z}{d_c}, \frac{d_c}{h}, Re, Mo, \theta, \frac{W}{d_c}, \frac{k_s'}{d_c}\right)$$

(1)

where C is the local void fraction, V is the local velocity, g is the gravity acceleration, d_c is the critical flow depth ($d_c = \sqrt[3]{Q^2/(g \times W^2)}$), Q is the water discharge, W is the channel width, h is the vertical step height, u' is a characteristic turbulent velocity, T_{int} is a turbulent time scale, L_{xz} is a turbulent length scale, x and y are the longitudinal and normal coordinates, Re is the Reynolds number, Mo is the Morton number

$Mo = g \times \mu^4 / (\rho \times \sigma^3)$, k_s' is the surface/skin roughness height. Equation (1) gives a dimensionless expression of the local air-water turbulent flow properties as functions of independent parameters that include both Froude and Reynolds numbers. Indeed the dimensionless discharge d_c/h is proportional to $Fr^{2/3}$.

In the present study, the same fluids (air and water) were used in model and prototype, and the Morton number became an invariant. Similarly, the chute slope θ, the channel width W, the step roughness k_s' were constant and the measurements were conducted on the channel centreline. That is, Equation (1) may be simplified into :

$$C, \frac{V}{\sqrt{g \times d_c}}, \frac{u'}{V}, T_{int} \times \sqrt{\frac{g}{d_c}}, \frac{L_{xz}}{d_c} = F\left(\frac{x}{d_c}, \frac{y}{d_c}, \frac{d_c}{h}, Re\right) \quad (2)$$

Equation (2) illustrates that the dynamic similarity of turbulent two-phase flows is not achievable with geometrically similar models because it is impossible to satisfy simultaneously both Froude and Reynolds similitudes in a geometrically-scaled model. It is well known, for example, that small size models underestimate the rate of air entrainment (Kobus 1984, Chanson 1997).

Herein both Froude and Reynolds similitudes were tested with respect to the two-phase flow properties, including the distributions of void fraction, bubble count rate, interfacial velocity, turbulence intensity and integral turbulent time and length scales. The experiments were conducted in a large size facility operating at large Reynolds numbers and the step cavity dimensions were scaled with a 2:1 undistorted geometric scaling ratio (Table 1). An alternative approach, based upon self-similarity considerations, was tested following Chanson and Carosi (2007).

	Series GH_06	Series FC_07
Triangular cavity dimensions (h×l):	0.10 m × 0.25 m	0.05 m × 0.125 m
Pseudo-bottom slope θ:	21.8°	21.8°
Chute width W (m):	1.0	1.0
Discharge Q (m³/s):	0.008 to 0.17	0.009 to 0.21
$d_c/h =$	0.18 to 1.57	0.4 to 3.5
Reynolds number Re:	3.2 E+4 to 7.1 E+5	3.5 E+4 to 8.3 E+5
Morton number Mo:	2.5 E-11	2.5 E-11

Table 1. Summary of experimental flow conditions.

Experimental Setup

New experiments were performed in the Gordon McKay Hydraulics Laboratory at the University of Queensland (Table 1). The experimental channel was previously used by Chanson and Toombes (2002) and Gonzalez (2005). The test section consisted of a 1 m wide, 0.6 m long broad-crested weir followed by a steep stepped section (step height h, step length l). In the first series of experiments (GH_06), the 1-m wide steep chute consisted of ten identical steps (h = 0.1 m, l = 0.25 m) made of marine ply. In the second series (FC_07), the steep channel had twenty identical steps (h = 0.05 m, l = 0.125 m).

Clear-water flow depths were measured with a point gauge. The water discharge was measured from the upstream head above the crest, and the head-discharge relationship was checked with detailed velocity distribution measurements on the crest itself (Gonzalez and Chanson 2007).

The two-phase flow properties were measured with either a single-tip conductivity probe, an array of two identical single-tip conductivity probes or a double-tip conductivity probe. Basic air-water flow measurements were performed with the single-tip conductivity probe (Fig. 3). Figure 3 illustrates the array of two single-tip probes side-by-side. The probe sensor consisted of a sharpened rod (0.35 mm ∅) coated with non-conductive epoxy set into a stainless steel surgical needle acting as the second electrode. Additional measurements were performed with a double-tip conductivity probe. The sensors consisted of a platinum wire (0.25 mm ∅) insulated except for its tip and set into a metal supporting tube. The probe sensors were aligned in the flow direction. The leading tip had a small frontal area (i.e. 0.05 mm²) and the trailing tip was laterally offset by 1.4 mm to avoid wake disturbance from the first tip. The longitudinal spacing between probe sensors was measured with a microscope: Δx = 7.0 mm. All the probes were excited by an electronic system (Ref. UQ82.518) designed with a response time less than 10 μs and calibrated with a square wave generator. The probe sensors were scanned at 20 kHz per sensor for 45 seconds per sensor at each sampling position.

Herein the measurements were conducted on the channel centreline (z = 0). With the array of single-tip conductivity probes, the second probe was placed beside the first one with the probe sensors at the same vertical and streamwise distances y and x respectively, but separated in the transverse direction by a known separation 3.6 mm ≤ Δz ≤ 60.3 mm (Fig. 3).
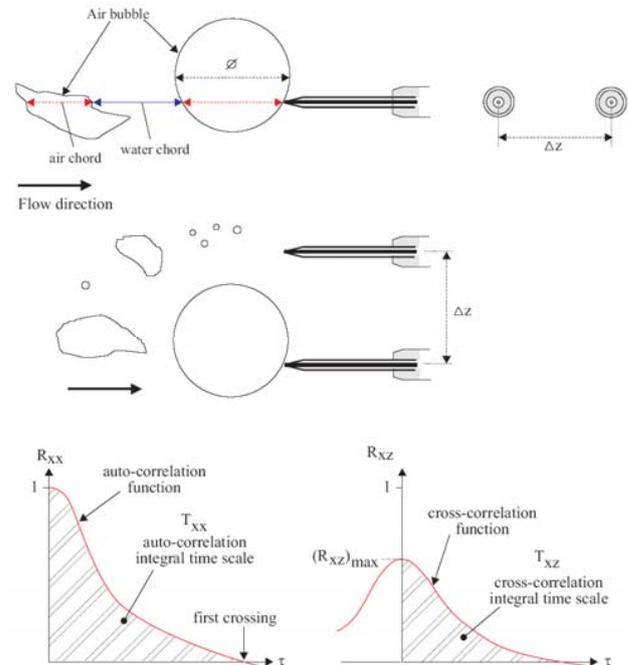

Fig. 3. Sketch of two single-tip probes side-by-side and the associated signal cross-correlation functions.

Signal processing

The measurement principle of a phase-detection conductivity probe is based upon the difference in electrical resistivity between air and water. The intrusive probe sensor is designed to pierce the bubbles and droplets. That is, the probe sensor must be sharpened and it must ideally face the stream of incoming bubbles as shown in Figure 3. The signal processing may be conducted on the raw signal output and on a thresholded "square wave" signal.

A thresholded signal analysis relies upon some arbitrary discrimination between the two phases. In high-velocity free-surface flows, a robust technique is the single threshold technique used herein. The resulting square-wave signal yields the instantaneous void fraction : C = 0 in water and C = 1 in air. It is used to calculate the time-averaged void fraction C, the bubble count rate F, the air/water chord times, the bubble/droplet chord lengths and their statistical moments (mean, median, std, skewness, kurtosis), and the streamwise particle grouping analysis.

The signal processing of the raw probe outputs is used for some

correlation analyses. These yield the time-averaged interfacial velocity V, the turbulence intensity Tu, the auto-correlation and cross-correlation integral time and length scales, the air-water integral length and time scales (Chanson and Carosi 2007). A further level of signal processing is the spectral analyses (Gonzalez 2005).

When two probe sensors are separated by a known transverse distance Δz, their signals may be analysed in terms of the auto-correlation and cross-correlation functions R_{xx} and R_{xz} respectively (Fig. 3). Basic correlation analysis results include the maximum cross-correlation coefficient $(R_{xz})_{max}$, and the auto- and cross-correlation time scales T_{xx} and T_{xz} (Fig. 3). The auto-correlation time scale T_{xx} represents an integral time scale of the longitudinal bubbly flow structure. The cross-correlation time scale T_{xz} is a characteristic time of the vortices with a length scale Δz advecting the air-water flow structures. Further, identical experiments with two probes were repeated herein with different separation distances Δz. The integral turbulent length and time scales (L_{xz} and T_{int} respectively) were calculated as :

$$L_{xz} = \int_{z=0}^{z=z((R_{xz})_{max}=0)} (R_{xz})_{max} \times dz \qquad (3)$$

$$T_{int} = \frac{1}{L_{xz}} \times \int_{z=0}^{z=z((R_{xz})_{max}=0)} (R_{xz})_{max} \times T_{xy} \times dz \qquad (4)$$

The length scale L_{xz} represents a measure of the transverse length scale of the large vortical structures advecting air bubbles and air-water packets (Chanson and Carosi 2007). The turbulent integral time scale T_{int} characterises the transverse time scale of the large eddies advecting the air bubbles.

Basic Flow Patterns
In the stepped chute, three basic flow regimes were observed depending upon the dimensionless discharge d_c/h. For small flow rates ($d_c/h < 0.5$), the waters flowed as a succession of free-falling nappes. For some intermediate discharges ($0.5 < d_c/h < 0.95$), the flow had a chaotic behaviour that was characteristic of a transition flow regime. For larger flows ($d_c/h > 0.95$), the waters skimmed above the pseudo-bottom formed by the step edges (Fig. 2). In the following paragraphs, the study is focused in the skimming flow conditions.

On the steep stepped chute, the waters were non-aerated at the upstream end of the chute (Fig. 1 and 2). Free-surface aeration occurred when the turbulent shear next to the free-surface exceeded the bubble resistance offered by surface tension and buoyancy. Downstream of the inception point of free-surface aeration, some strong air-water mixing took place. Large amounts of air were entrained, and very-strong interactions between main stream turbulence, step cavity recirculation zones and free-surface were observed associated with strong energy dissipation and flow resistance

The location L_I of the inception point of free-surface aeration was recorded during both experimental series (Table 1). The data were compared successfully with earlier studies (Chanson 1995, 2001). For the present study, the results were best correlated by :

$$\frac{L_I}{h \times \cos\theta} = 1.05 + 5.11 \times \frac{q}{\sqrt{g \times \sin\theta \times (h \times \cos\theta)^3}}$$

$$0.4 < d_c/h < 3.4 \qquad (5)$$

where $q = Q/B$ is the water discharge per unit width. Equation (5) is valid for both step heights $h = 0.05$ and 0.10 m on the 22° stepped chute only. Overall the present results were very close to the earlier observations of Chanson and Toombes (2002) and Gonzalez (2005) in the same chute.

Experimental Results: (1) Air-Water Flow Properties
Distributions of void fraction and bubble count rate
The experiments highlighted some substantial free-surface aeration at and immediately downstream of the inception point of

free-surface aeration, while the flow aeration remained sustained downstream. Figure 4 illustrates typical dimensionless distributions of void fraction and bubble count rate downstream of the inception point. For that discharge, the flow aeration was nil at step edge 12, immediately upstream of the inception point. Between step edges 13 and 14, some strong self-aeration took place, and the amount of entrained air and the mean air content were about constant between the step edges 16 and 20 (Fig. 5).
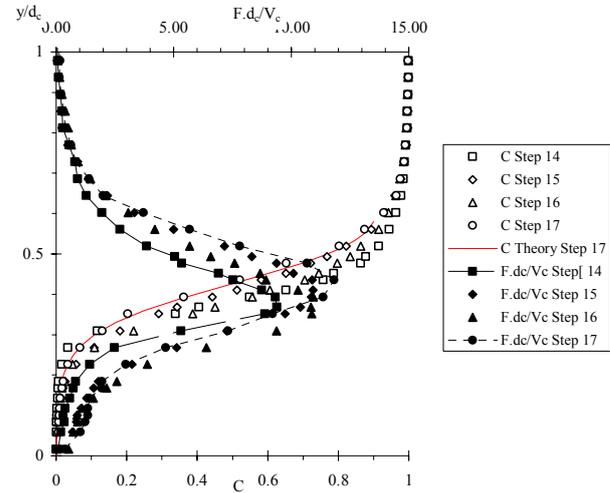
Fig. 4. Dimensionless distributions of void fraction C and bubble count rate $F \times d_c/V_c$. Flow conditions: $d_c/h = 2.39$, Re $= 5.1\ 10^5$, h $= 0.05$ m, single-tip conductivity probe ($\varnothing = 0.35$ mm).
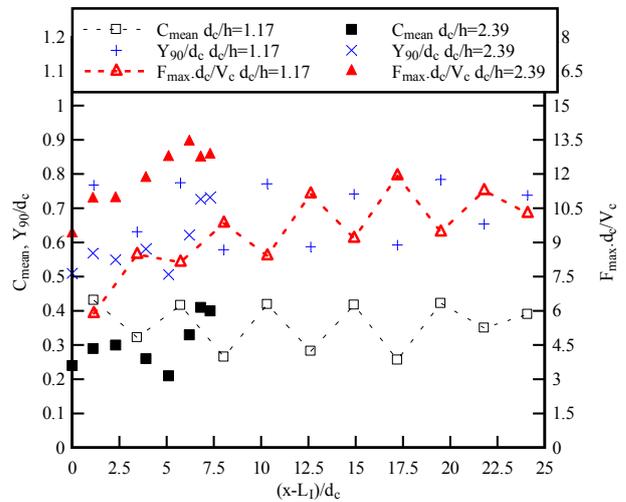
Fig. 5. Longitudinal distributions of depth-averaged void fraction C_{mean}, characteristic depth Y_{90}/d_c and bubble count rate $F_{max} \times d_c/V_c$. Flow conditions: $d_c/h = 1.17$ & 2.39, h $= 0.05$ m.

In skimming flows, the void fraction distributions followed closely the analytical solutions of the advective diffusion for air bubbles:

$$C = 1 - \tanh^2 \left(K' - \frac{y'}{2 \times D_o} + \frac{\left(y' - \frac{1}{3}\right)^3}{3 \times D_o} \right) \qquad \text{at step edges} \quad (6)$$

where C is the void fraction, $y' = y/Y_{90}$, y is distance measured normal to the pseudo-invert, Y_{90} is the characteristic distance where C = 90% (Chanson and Toombes 2002). K' is an integration constant and D_o is a function of the depth-averaged void fraction C_{mean} only :

$$K' = 0.32745 + 12 \times D_o - 881 \times D_o \qquad (7)$$
$$C_{mean} = 0.762 \times (1.0434 - exp(-3.614 \times D_o)) \qquad (8)$$
where the depth-averaged void fraction C_{mean} is defined in terms of the characteristic distance where C = 90%:

$$C_{mean} = \int_0^1 (1-C) \times dy' \qquad (9)$$

Equation (6) is compared with experimental data in Figure 4.

The dimensionless distributions of bubble count rate showed consistently a characteristic shape with a maximum value F_{max} observed for void fractions between 0.40 and 0.55. This is seen in Figure 4, where the upper horizontal axis $F \times d_c/V_c$ is the dimensionless bubble count rate and dotted connecting lines were added for two step edges.

Some longitudinal distributions of maximum bubble count rate $F_{max} \times d_c/V_c$ are presented in Figure 5, together with the depth-averaged void fraction C_{mean} and the characteristic depth Y_{90}/d_c. In Figure 5, the horizontal axis $(x-L_I)/d_c$ is the dimensionless distance from the inception point. A characteristic feature of all the experiments was a distinct seesaw pattern in terms of both $F_{max} \times d_c/V_c$ and C_{mean}. This oscillating pattern had a wave length of about two step cavities (Fig. 5). Such a pattern was observed before for a range of slopes and step heights (Boes 2000, Chanson and Toombes 2002, Yasuda and Chanson 2003). It is believed to result from strong interferences between vortex shedding in the shear layers behind each step edge and the free-surface.

Another feature, seen in Figure 5, is that the two-phase flow properties did not reach uniform equilibrium before the end of the chute. For example, the dimensionless maximum bubble count rate increased sharply with longitudinal distance immediately downstream of the inception point (i.e. $(x-L_I)/d_c <$ 10), while it continued to increase gradually with increasing distance further downstream (Fig. 5). Such a pattern was seen for all the experiments (Table 1).

Distributions of interfacial velocity and turbulence intensity

The dimensionless distributions of interfacial velocity and turbulent intensity showed some characteristic shapes. At each step edge, the velocity distributions compared favourably with a power-law function for $y/Y_{90} < 1$ and with an uniform profile for $y/Y_{90} > 1$:

$$\frac{V}{V_{90}} = y'^{1/N} \qquad (10)$$

$$\frac{V}{V_{90}} = 1 \qquad (11)$$

where V_{90} is the characteristic air-water velocity at $y = Y_{90}$. Several studies yielded Equation (10) (e.g. Matos 2000, Boes 2000, Chanson and Toombes 2002, Gonzalez and Chanson 2004), but a few documented the velocity distribution in the upper spray region (Chanson and Carosi 2007). Equations (10) and (11) are compared with experimental data in Figure 6. In the present study, the velocity power law exponent was 1/10 in average (i.e. N = 10), although it varied between adjacent step edges. Such fluctuations were believed to be caused by some complicated interference between adjacent shear layers and cavity flows.

The distributions of turbulence intensity Tu showed a distinct shape with a maximum turbulence Tu_{max} for C = 0.4 to 0.6 (Fig. 6). Typical longitudinal distributions of both maximum turbulence intensity Tu_{max} and characteristic velocity V_{90}/V_c are shown in Figure 7 for two flow rates. The data exhibited a distinctive seesaw pattern, and the finding was observed for all investigated discharges. This seesaw feature was linked with the distinct seesaw pattern in terms of the maximum bubble count rate (Fig. 5). It is believed that the longitudinal seesaw patterns in terms of $F_{max} \times d_c/V_c$, V_{90}/V_c and Tu_{max} were a characteristic

feature of the skimming flows above the triangular cavities. It was linked with the interactions between cavity recirculations and mainstream, and interactions between adjacent cavity flows.

In skimming flows, the basic mechanisms of turbulent dissipation included cavity recirculation, momentum exchange with the free stream, and interactions between free-surface and mainstream turbulence. The interactions between mixing layer and horizontal step face, and skin friction at the step downstream end contributed to further energy dissipation on moderate slopes similar to the present configurations. At each step edge, highly coherent small-scale vortices were formed abruptly at the step corner because of the large gradient of vorticity at the corner. The initial region of the mixing layer was dominated by a train of sequential small-scale vortices which eventually paired to form large scale vortical structures that are advected downstream. The three dimensional nature of recirculating vortices is believed to play a role to further the rate of energy dissipation (Gonzalez 2005). Gonzalez and Chanson (2004) demonstrated quantitatively means to enhance the flow resistance with turbulence manipulation of the cavity recirculation.
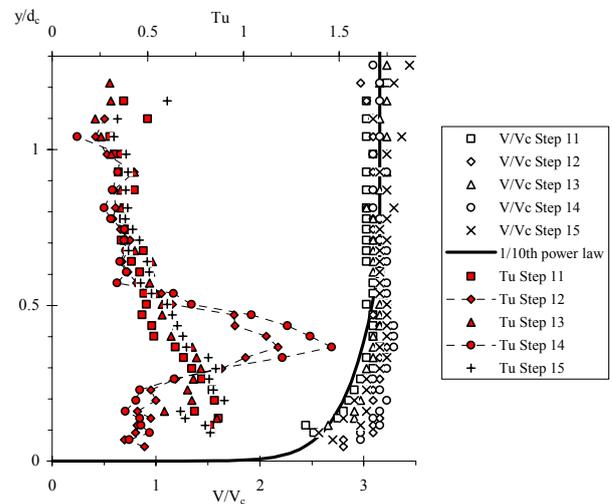

Fig. 6. Dimensionless distributions of interfacial velocity V/V_c and turbulence intensity Tu. Flow conditions: $d_c/h = 1.75$, Re = 3.1×10^5, h = 0.05 m, double-tip conductivity probe ($\varnothing = 0.25$ mm).
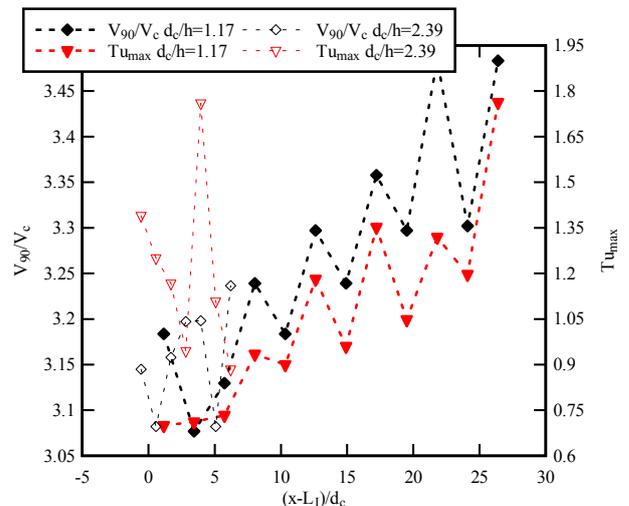

Fig. 7. Longitudinal distributions of characteristic air-water velocity V_{90}/V_c and maximum turbulence level Tu_{max}. Flow conditions: $d_c/h = 1.17$ & 2.39, h = 0.05 m.

Probability distribution functions of bubble and droplet chords

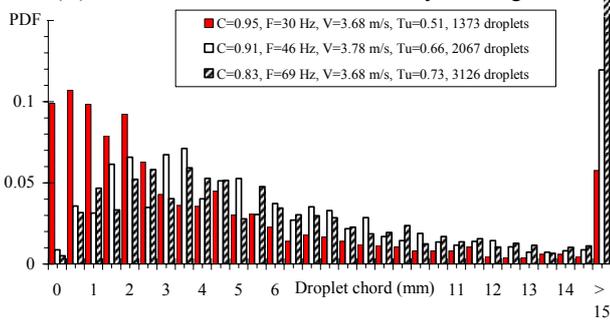The probability distribution functions of particle chords were investigated in terms of bubble chords in the bubbly flow (C < 0.3) and in terms of droplet chord lengths in the spray region (C > 0.7). Typical results are presented in Figure 8. For each graph, the legend provides the local air-water flow properties and the histogram columns represent the probability of chord sizes in a 0.5 mm chord interval. The probability of chords between 1 and 1.5 mm is represented by the column labelled 1 mm. Chord sizes larger than 15 mm are regrouped in the last column (> 15).

In the bubbly flow region (C < 0.3), the probability distribution functions showed a broad spectrum of bubble chords at each location (Fig. 8A). The range of bubble chord extended from less than 0.3 mm to more than 15 mm. The bubble chord size distributions were skewed with a preponderance of small bubbles relative to the mean. In Figure 8A, the mode of the probability distribution function was observed for chords between 0.5 and 2 mm. The probability distribution functions of bubble chord tended to follow a log–normal distribution at all locations and for all discharges. The result was consistent with the earlier data of Chanson and Toombes (2002) and Gonzalez and Chanson (2004) in skimming flows.

In the spray region, the probability distribution functions of drop sizes showed also a wide range of droplet chords at each location (Fig. 8B). While the droplet chord size distributions were skewed with a preponderance of small droplets, the probability density function was flatter and broader than that of the bubble chords (Fig. 8). In the upper spray region (C > 0.95 to 0.97), the probability distribution functions were flat and did not follow a log-normal distribution.
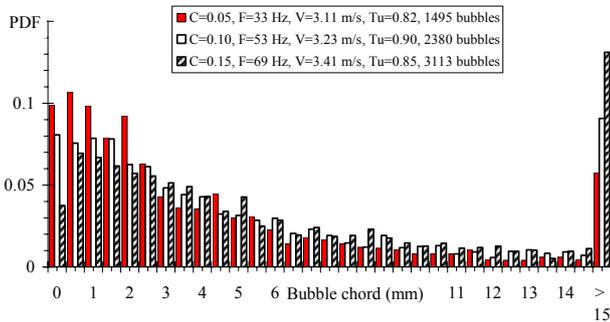
(A) Air bubble chord sizes in the bubbly flow region.

(B) Water droplet chord sizes in the spray region.
Fig. 8. Probability distribution functions of bubble and droplet chord sizes in a skimming flow. Flow conditions: $d_c/h = 2.71$, h = 0.05 m, Re = 6.9 10^5, Step 17, double-tip conductivity probe ($\varnothing$=0.25 mm).

Experimental Results: (2) Turbulent Time and Length Scales

Some experiments were conducted with an array of two identical sensors ($\varnothing$ = 0.35 mm) separated by a transverse distance Δz and they were repeated for several separation distances (Tables 2 and

3). Tables 2 and 3 (Appendix I) list the experimental conditions and summarise some key results. Typical distributions of auto-correlation time scale T_{xx}, cross-correlation time scale T_{xz} and maximum cross-correlation coefficient $(R_{xz})_{max}$ are presented in Figure 9 and compared with the distribution of void fraction. The cross-correlation time scale and maximum cross-correlation coefficient data were obtained for a transverse separation distance $\Delta z = 8.5$ mm.

The experimental results showed similar shapes of the auto- and cross-correlation time scale distributions in the bulk of the flow (C < 0.9). The auto-correlation time scales T_{xx} (symbols ×) exhibited however a different trend in the upper spray region. This is seen in Figure 9 for $y/d_c > 0.7$. This was linked with a different spray structure with the upper spray region (C > 0.95). For C > 0.95, the spray consisted primarily of ejected droplets that did not interact with the rest of the flow.

For all flow conditions and at each step edge, the distributions of cross-correlation time scale T_{xz} and maximum cross-correlation coefficient $(R_{xz})_{max}$ presented some maxima in the intermediate region (0.3 < C < 0.7). The corresponding maxima are reported in Appendix I.
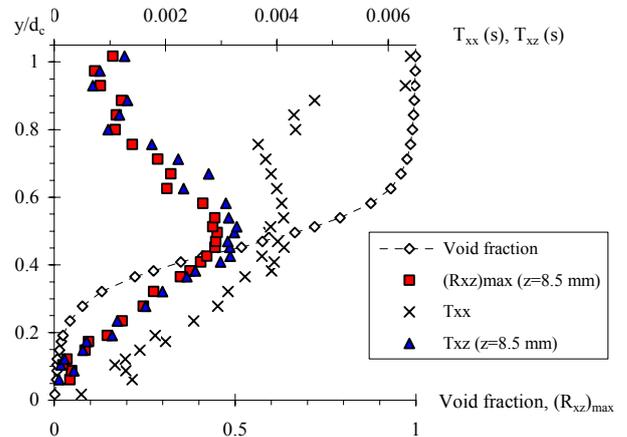

Fig. 9. Distributions of void fraction, maximum cross-correlation coefficient $(R_{xz})_{max}$, auto-correlation time scale T_{xx} and cross-correlation time scale T_{xz} in skimming flows. Flow conditions: $d_c/h = 2.39$, h = 0.05 m, Re = 4.9 10^5, Step 17, $\Delta z = 8.5$ mm, single-tip conductivity probe ($\varnothing$=0.35 mm).

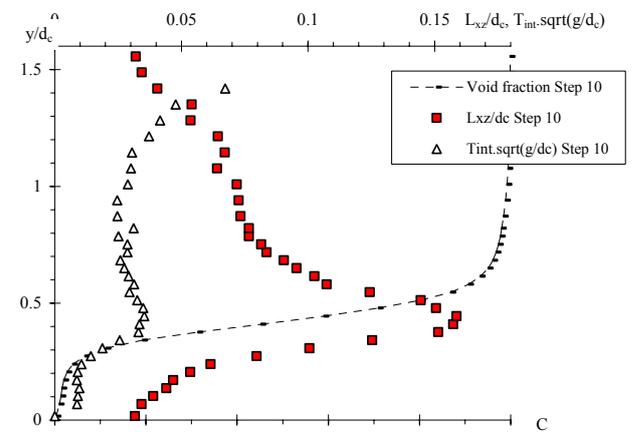Fig. 10. Dimensionless distributions of integral turbulent length and time scales, L_{xz}/d_c and $T_{int} \times \sqrt{g/d_c}$, and void fraction in skimming flows. Flow conditions: $d_c/h = 1.15$, h = 0.05 m, Re = 1.7 10^5, Step 10, single-tip conductivity probe ($\varnothing$=0.35 mm).

The integral turbulent length and time scales, L_{xz} and T_{int} respectively, were calculated using Equations (3) and (4). Typical results in terms of dimensionless turbulent length and time scales, L_{xz}/d_c and $T_{int} \times \sqrt{g/d_c}$, are presented in Figure 10. The measured void fraction data are shown for completeness.

In bubbly flows, the turbulent length scales were closely linked with the characteristic sizes of the large-size eddies entrapping air bubbles, as illustrated by series of high-speed photographs (e.g. Hoyt and Sellin 1989, Chanson 1997). Herein the integral turbulent length scale L_{xz} characterised the transverse size of the large eddies advecting the air bubbles and air-water packets. The present findings emphasised the existence of large-scale turbulent structures in the intermediate zone $(0.3 < C < 0.7)$ between the bubbly flow and spray regions (Fig. 10). It is hypothesised that these large vortices may have a preponderant role in terms of turbulent dissipation. The integral turbulent length scales satisfied: L_{xz}/d_c = 0.04 to 0.16 (Fig. 10). The result was irrespective of the dimensionless flow rate d_c/h and step height within the range of the experiments (Table 1). The associated turbulence time scale T_{int} was a measure of the integral time scale of the large vortices, and the results yielded: $0.005 \leq T_{int} \times \sqrt{g/d_c} \leq 0.05$.

The high-velocity open channel flows on the stepped channel were highly turbulent. The present results demonstrated that the high levels of turbulence were associated directly with some large scale turbulence. In particular, the intermediate region $(0.3 < C < 0.7)$ between the bubbly and spray regions seemed to play a major role in the development the large eddies and turbulent dissipation. Turbulence level maxima were observed consistently for $0.4 < C < 0.5$, while maximum integral turbulent scales were seen for $0.5 < C < 0.7$. The present findings implied that, while the stepped cavities contributed to intense turbulence production, some turbulent energy was dissipated in the form of large-scale vortices in the bulk of the flow. The dissipated energy contributed to the entrapment and advection of air bubbles within the main flow, as well as to the formation of water droplets and their ejection above the free-surface. The mechanisms were consistent with the experimental results of Gonzalez and Chanson (2004) who observed that some increased rate of energy dissipation induced by passive turbulent manipulation was linked with a greater spray production.

Dynamic Similarity
The validity of both Froude and Reynolds similitudes were tested with respect to the two-phase flow properties, including the distributions of void fraction, bubble count rate, interfacial velocity, turbulence intensity and integral turbulent time and length scales. The experimental program covered two step cavity dimensions scaled with a 2:1 undistorted geometric scaling ratio (Table 1)

<u>Froude similitude</u>
Overall the comparative results showed that the distributions of void fraction were properly scaled with a Froude similitude, for the investigated flow conditions (Table 1). This is illustrated in Figure 11 showing dimensionless distributions of void fraction. In addition, the void fraction distributions compared well with an analytical solution of the advection diffusion equation for air bubbles (Chanson and Toombes 2002). Good agreement was observed also in terms of dimensionless distributions of velocity (Fig. 12), as well as in terms of mean air content C_{mean}, and dimensionless air-water flow velocity V_{90}/V_c.
Significant differences, hence scale effects, were observed in terms of dimensionless distributions of bubble count rates $F \times d_c/V_c$ and of turbulence intensity Tu (Fig. 11 and 12). Typically lesser dimensionless bubble count rates by about 30 to 60% were observed with the smallest step height. This is

illustrated in Figure 11, and the finding implied significant scale effects in terms of number of entrained bubbles and bubble sizes. Further scale effects in terms of turbulence intensity distributions were observed consistently with lesser maximum turbulence levels for the smallest step height (h = 0.05 m). This is well illustrated in Figure 12. A comparative analysis of bubble chord size distributions, for similar flow rate, identical location and local void fraction, showed consistently differences: the entrained bubbles were comparatively larger for the smallest model. A similar observation was made in terms of water droplet size distributions in the spray region. In dimensional terms, the size distributions of the smallest bubbles and droplets were about the same for both step heights, but a broader range of large particles were seen with the largest step height (h = 0.1 m).

The present results, obtained with a 22° slope, supported the earlier findings of Chanson and Gonzalez (2005) with 3.4° and 16° slope stepped chutes.
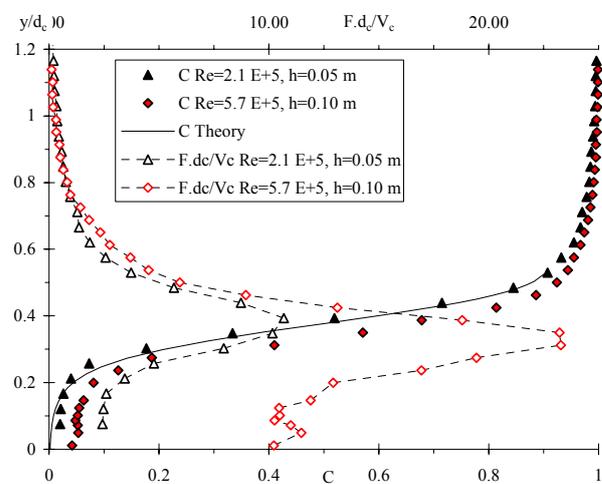

Fig. 11. Dimensionless distributions of void fraction C and bubble count rate $F \times d_c/V_c$. Flow conditions: d_c/h = 1.32, h = 0.05 & 0.10 m, Re = 2.1 10^5 & 5.7 10^5, Step 10, double-tip conductivity probe ($\varnothing$=0.25 mm).
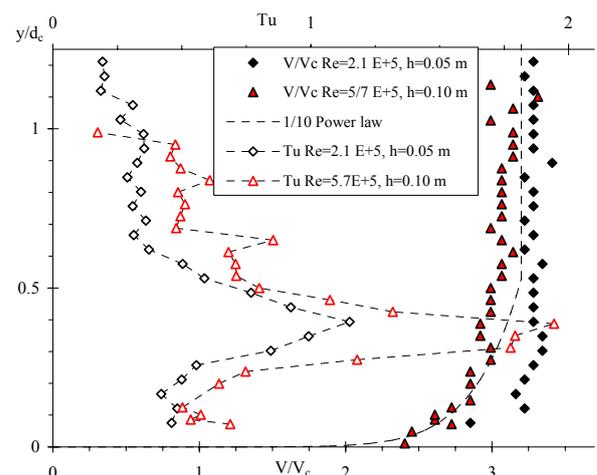

Fig. 12. Dimensionless distributions of interfacial velocity V/V_c and turbulence intensity Tu. Flow conditions: d_c/h = 1.32, h = 0.05 & 0.10 m, Re = 2.1 10^5 & 5.7 10^5, Step 10, double-tip conductivity probe ($\varnothing$=0.25 mm).

Scale effects were also observed in terms of dimensionless distributions of integral turbulent length and time scales (Fig. 13). Typically larger dimensionless turbulent scales were observed with the smallest step height. This is illustrated in Figure 13, and

the finding implied some scale effects in terms of the large vortical structures advecting the turbulence.

In summary, the results showed a lesser number of entrained bubbles and comparatively greater bubble sizes observed in the smallest flumes, as well as lower turbulence levels and larger turbulent length and time scales. The findings have direct implications on stepped spillway design. Lesser turbulence levels in small laboratory flumes must imply a lesser rate of energy dissipation, particularly on long chutes. That is, small-size models are likely to underestimate the rate of energy dissipation of prototype stepped spillways for similar flow conditions. Similarly, the lesser number of entrained bubble sizes in laboratory flumes must affect the rate of air-water mass transfer on the chute. Present results imply that the air-water interface area, hence the rate of air-water mass transfer, are underestimated in small-size physical-models, and extrapolation are not reliable unless working at full scale (Toombes and Chanson 2005).
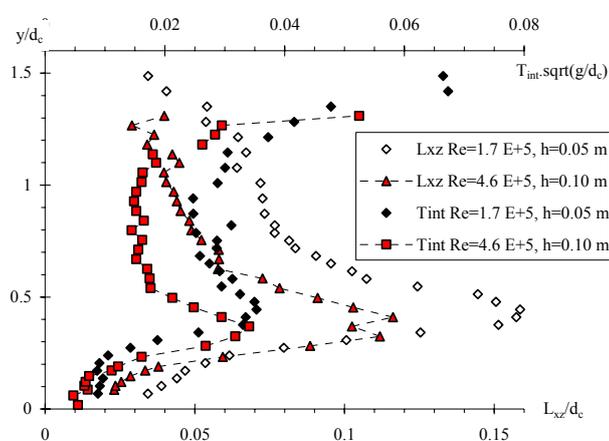

Fig. 13. Dimensionless distributions of integral turbulent length L_{xz}/d_c and time $T_{int} \times \sqrt{g/d_c}$ scales. Flow conditions: $d_c/h = 1.15$, h = 0.05 & 0.10 m, Re = 1.7×10^5 & 4.6×10^5, Step 10, single-tip conductivity probe ($\varnothing = 0.35$ mm).

Reynolds similitude

A systematic comparison of the two-phase flow properties was conducted with identical Reynolds numbers (i.e. identical flow rates) between the two cavity sizes. The results showed that the data with largest Froude number d_c/h (i.e. smallest cavity size) exhibited smaller dimensionless bubble count rates, lesser turbulence levels, all other parameters being constant. The distributions of integral turbulent length and time scales presented some differences.

Altogether the data showed that the Reynolds similitude was not valid in these complicated two-phase flow properties.

Self-similarity

In fluid mechanics, many types of flow motion present some form of self-similarity. (Barenblatt 1996). Self-similarity is a powerful tool in turbulence flow research and high-velocity air-water flows. The non-linear interactions between vortices and entrained air bubbles at different scales lead usually to a complex gas-liquid flow structure. Thus relationships at different scales are of crucial significance in understanding and controlling these flows. Following the approach of Chanson and Carosi (2007), self-similarity was observed herein in terms of the air-water flow properties. Self-similar relationships were observed at both macroscopic and microscopic levels. For example, the distributions of void fraction and interfacial velocity at a macroscopic level; the cross-correlation function and probability distribution functions of particle chords at a microscopic level.

Self-similarity is closely linked with dynamic similarity. Equations (1) and (2) showed that it is nearly impossible to achieve a true dynamic similarity in small-size models of high-velocity air-water flows because of number of relevant dimensionless parameters. The present experimental results showed a number of self-similar relationships that remain invariant under changes of scale. For example, Equations (6), (10) and (11). These relationships have scaling symmetry which led in turn to remarkable application at prototype scales. The results are significant because they demonstrate a number of self-similar relationships characterising the air-water flow properties in a complex high-velocity flow. They provide a picture general enough to be used, as a first approximation, to characterise the air-water flow field in similar stepped spillway prototype structures.

Summary and Conclusion

Two-phase flow properties were measured in high-velocity open channel flows above triangular cavities. Detailed turbulence data were collected in a large-size facility, including turbulence levels and turbulent time and length scales. The measurements were conducted with two cavity sizes and several discharges. The results were used to test the validity of the Froude and Reynolds similarities.

The results showed consistently that the Froude similitude was not satisfied using a 2:1 geometric scaling ratio. Lesser number of entrained bubbles and comparatively greater bubble sizes were observed at the smaller Reynolds numbers, as well as lower turbulence levels and larger turbulent length and time scales. In practical terms, small-size models did underestimate the rate of energy dissipation and the aeration efficiency of prototype stepped spillways for similar flow conditions. Similarly a Reynolds similitude was tested. The results showed also some significant scale effects. The present results showed however a number of self-similar relationships that remained invariant under changes of scale and confirmed the analysis of Chanson and Carosi (2007). The present findings are significant and suggest that self-similarity may provide a picture general enough to be used to characterise the air-water flow field in large prototype channels.

References
[1] Barenblatt, G.I. (1996). "Scaling, Self-Similarity, and Intermediate Asymptotics." Cambridge University Press, UK, 386 pages.
[2] Boes, R.M. (2000). "Zweiphasenstroömung und Energieumsetzung an Grosskaskaden." Ph.D. thesis, VAW-ETH, Zürich, Switzerland (in German). (also Mitteilungen der Versuchsanstalt fur Wasserbau, Hydrologie und Glaziologie, ETH-Zurich, Switzerland, No. 166).
[3] Brocchini, M., and Peregrine, D.H. (2002). "Interaction of Strong Turbulence with Free Surfaces", World Scientific, Advances in Coastal and Ocean Engineering Series, Vol. 8, Singapore.
[4] Cain, P., and Wood, I.R. (1981). "Measurements of Self-aerated Flow on a Spillway." Journal Hydraulic Division, ASCE, 107, HY11, pp. 1425-1444.
[5] Chanson, H. (1995). "Hydraulic Design of Stepped Cascades, Channels, Weirs and Spillways." Pergamon, Oxford, UK, Jan., 292 pages.
[6] Chanson, H. (1997). "Air Bubble Entrainment in Free-Surface Turbulent Shear Flows." Academic Press, London, UK, 401 pages.
[7] Chanson, H. (2001). "The Hydraulics of Stepped Chutes and Spillways." Balkema, Lisse, The Netherlands, 418 pages.

[8] Chanson, H., and Carosi, G. (2007). "Turbulent Time and Length Scale Measurements in High-Velocity Open Channel Flows." Experiments in Fluids, Vol. 42, No. 3, pp. 385-401 (DOI 10.1007/s00348-006-0246-2).

[9] Chanson, H., and Gonzalez, C.A. (2005). "Physical Modelling and Scale Effects of Air-Water Flows on Stepped Spillways." Journal of Zhejiang University SCIENCE, Vol. 6A, No. 3, March, pp. 243-250.

[10] Chanson, H., and Toombes, L. (2002). "Air-Water Flows down Stepped Chutes : Turbulence and Flow Structure Observations." International Journal of Multiphase Flow, Vol. 28, No. 11, pp. 1737-1761.

[11] Felder, S., and Chanson, H. (2007). "Turbulence and Turbulent length and Time Length Scales in Skimming Flows on a Stepped Spillway. Dynamic Similarity, Physical Modelling and Scale Effects." Report No. CH64/07, Div. of Civil Engineering, The University of Queensland, Brisbane.

[12] Gonzalez, C.A. (2005). "An Experimental Study of Free-Surface Aeration on Embankment Stepped Chutes." Ph.D. thesis, Department of Civil Engineering, The University of Queensland, Brisbane, Australia, 240 pages.

[13] Gonzalez, C., and Chanson, H. (2004). "Effects of Turbulence Manipulation in Skimming Flows: An Experimental Study." Proc. 15th Australasian Fluid Mech. Conf., AFMC, Sydney, Australia, Paper AFMC00104, 4 pages (CD-ROM).

[14] Gonzalez, C.A., and Chanson, H. (2005). "Experimental Measurements of Velocity and Pressure Distribution on a Large Broad-Crested Weir." Flow Measurement and Instrumentation, Vol. 18, No. 3-4, pp. 107-113 (DOI 10.1016/j.flowmeasinst.2007.05.005).

[15] Kobus, H. (1984). "Scale Effects in Modelling Hydraulic Structures." Proc. Intl Symp. on Scale Effects in Modelling Hydraulic Structures, IAHR, Esslingen, Germany.

[16] Matos, J. (2000). "Hydraulic Design of Stepped Spillways over RCC Dams." Intl Workshop on Hydraulics of Stepped Spillways, Zürich, Switzerland, Balkema Publ., pp. 187-194.

[17] Rao, N.S.L., and Kobus, H.E. (1971). "Characteristics of Self-Aerated Free-Surface Flows." Water and Waste Water/Current Research and Practice, Vol. 10, Eric Schmidt Verlag, Berlin, Germany.

[18] Straub, L.G., and Anderson, A.G. (1958). "Experiments on Self-Aerated Flow in Open Channels." Jl of Hyd. Div., Proc. ASCE, Vol. 84, No. HY7, paper 1890, pp. 1890-1 to 1890-35.

[19] Toombes, L., and Chanson, H. (2005). "Air-Water Mass Transfer on a Stepped Waterway." Jl of Environ. Engrg., ASCE, Vol. 131, No. 10, pp. 1377-1386.

[20] Wood, I.R. (1991). "Air Entrainment in Free-Surface Flows." IAHR Hydraulic Structures Design Manual No. 4, Hydraulic Design Considerations, Balkema Publ., Rotterdam, The Netherlands, 149 pages.

[21] Yasuda, Y., and Chanson, H. (2003). "Micro- and Macroscopic Study of Two-Phase Flow on a Stepped Chute." Proc. 30th IAHR Biennial Congress, Thessaloniki, Greece, Vol. D, pp. 695-702

Appendix I

d_c/h	Step	Δz (mm)	Max($(R_{xz})_{max}$)	Max(T_{xz}) (s)
1.15	10	0	1 (+)	0.0053 (+)
		3.6	0.6339	0.005
		6.3	0.4504	0.0037
		8.45	0.4293	0.0039
		10.75	0.3914	0.0038
		13.7	0.3172	0.0041
		16.7	0.3215	0.0039
		21.7	0.2391	0.0027
		29.5	0.182	0.0023

d_c/h	Step	Δz (mm)	Max($(R_{xz})_{max}$)	Max(T_{xz}) (s)
		40.3	0.1516	0.0023
1.45	10	0	1 (+)	0.0055 (+)
		3.6	0.6493	0.0048
		8.45	0.468	0.0041
		13.7	0.37	0.0044
		21.7	0.2845	0.0040
		40.3	0.1417	0.0020
		55.7	0.1166	0.0019

Table 2. Experimental observations (Series 1, h = 0.10 m) of maxima of transverse cross-correlation time scale T_{xz} and of maximum cross-correlation $(R_{xz})_{max}$ in a cross-section as functions of the transverse separation distance. Note: (+) : auto-correlation result.

d_c/h	Step	Δz (mm)	Max($(R_{xz})_{max}$)	Max(T_{xz}) (s)
1.17	10	0	1 (+)	0.0040 (+)
		3.7	0.567	0.0036
		5.2	0.474	0.0033
		8.2	0.335	0.0027
		11.4	0.257	0.0024
		15.2	0.198	0.0019
		19.6	0.172	0.0014
		24.8	0.114	0.0010
		29.9	0.075	0.0007
		35.4	0.053	0.0008
		40.1	0.035	0.0003
		45.6	0.022	0.0003
1.17	18	0	1 (+)	0.0056 (+)
		3.7	0.624	0.0053
		5.2	0.577	0.0052
		8.2	0.444	0.0044
		11.4	0.379	0.0040
		15.2	0.331	0.0035
		19.6	0.276	0.0033
		24.8	0.234	0.0028
		29.9	0.178	0.0021
		35.4	0.154	0.0021
		40.1	0.137	0.0020
		45.6	0.121	0.0018
2.39	17	0	1 (+)	0.0041 (+)
		3.6	0.719	0.0039
		5.1	0.614	0.0037
		8.5	0.451	0.0033
		11.7	0.368	0.0031
		15.9	0.305	0.0026
		20.8	0.239	0.0023
		26.7	0.118	0.0009
		34.3	0.156	0.0017
		42.4	0.119	0.0014
		50.9	0.096	0.0012
		60.3	0.073	0.0012
2.39	20	0	1 (+)	0.0034 (+)
		3.6	0.668	0.0031
		5.1	0.550	0.0029
		8.5	0.367	0.0026
		11.7	0.288	0.0021
		15.9	0.204	0.0017
		20.8	0.149	0.0014
		26.7	0.118	0.0009
		34.3	0.082	0.0008
		42.4	0.073	0.0006
		50.9	0.053	0.0006
		60.3	0.041	0.0005
3.05	20	0	1 (+)	0.0036 (+)
		3.5	0.729	0.0033
		5.1	0.534	0.0027
		8.5	0.392	0.0025
		11.7	0.308	0.0021
		15.9	0.221	0.0018
		20.8	0.184	0.0015
		26.7	0.158	0.0011
		34.3	0.108	0.0010
		42.4	0.089	0.0009
		50.9	0.069	0.0006
		60.3	0.049	0.0005

Table 3. Experimental observations (Series 2, h = 0.05 m) of maxima of transverse cross-correlation time scale T_{xz} and of maximum cross-correlation $(R_{xz})_{max}$ in a cross-section as functions of the transverse separation distance. Note: (+) : auto-correlation result.